Advanced Energy Materials

ADVANCED ENERGY MATERIALS
www.advenergymat.de

RESEARCH ARTICLE OPEN ACCESS

Engineering Na-Rich P2-Type Layered Oxides Through Li/Ti Dual Doping for Oxygen Redox Activation and Superior Structural Stability

Rishika Jakhar[1] | Shrestha Ghosh[2] | Adesh Rohan Mishra[3] | Shristi Pradhan[4] | Debalina Sarkar[2,10] | Yuanlong Bill Zheng[1] | Zengqing Zhuo[5] | Tianyi Li[6] | Lu Ma[7] | Minghao Zhang[1] | Shyue Ping Ong[3,11] | Matthew Li[8] | Leeann Sun[1] | Prabhat Thapliyal[9] | Jing Wang[1] | Abhik Banerjee[2,10] | Ying Shirley Meng[1,3]

[1]Pritzker School of Molecular Engineering, The University of Chicago, Chicago, Illinois, USA | [2]Research Institute for Sustainable Energy, Center for Research and Education in Science and Technology (TCG CREST), Kolkata, India | [3]Aiiso Yufeng Li Family Department of NanoEngineering, University of California San Diego, La Jolla, California, USA | [4]Department of Chemistry, University of Illinois Chicago, Chicago, Illinois, USA | [5]Advanced Light Source, Lawrence Berkeley National Laboratory, Berkeley, California, USA | [6]Advanced Photon Source, Argonne National Laboratory, Lemont, Illinois, USA | [7]National Synchrotron Light Source II, Brookhaven National Laboratory, Upton, New York, USA | [8]Chemical Sciences and Engineering, Argonne National Laboratory, Lemont, Illinois, USA | [9]Department of Chemistry, Universität Bayreuth, Bayreuth, Germany | [10]Academy of Scientific and Innovative Research (AcSIR), Ghaziabad, India | [11]Department of Materials Science and Engineering, National University of Singapore, Singapore

Correspondence: Jing Wang (wangj467@uchicago.edu) | Abhik Banerjee (abhik.banerjee@tcgcrest.org) | Ying Shirley Meng (shirleymeng@uchicago.edu)

Received: 30 October 2025 | **Revised:** 22 January 2026 | **Accepted:** 30 January 2026

Keywords: cation doping | oxygen redox | Sodium cathode | Transition-metal-oxygen covalency

ABSTRACT

Sodium layered oxides Na_xMO_2 ($x \leq 1$ and M = transition metal ions) have gained significant interest as sodium-ion battery (NIB) cathodes owing to their high operating voltages and potential for higher energy density compared with polyanion and Prussian blue–type cathodes. However, their practical applications are often hindered by the irreversible structural transitions leading to capacity fading during cycling. The nature and substitution of transition metal ions define the material properties and electrochemical performance. In this study, through comprehensive electrochemical characterization combined with multi-scale structural and spectroscopical analyses, we demonstrate the synergistic impacts of Lithium and Titanium doping, which not only increases overall capacity by boosting cation and anion cooperative redox contributions but also improves the rate capability and cycling stability. Specifically, Li^+ doping enhances the available sodium inventory for extraction, while Ti^{4+} disrupts Na^+/vacancy ordering at lower voltages (< 4 V) and mitigates the detrimental P2→OP4/O2 phase transition during cycling. The combined effect of Lithium and Titanium doping promotes more charge localization on Oxygen, which activates reversible lattice oxygen redox reactions at elevated voltages, contributing additional capacity beyond conventional cationic redox. This work provides crucial insights into the design of high-performance, high-capacity P2-type layered cathode materials for sodium-ion batteries.

1 | Introduction

Lithium-ion batteries (LIBs) have seamlessly integrated into many aspects of modern life and are poised to drive the electrified future, representing a transformative technology for the global economy [1]. However, the limited abundance of Lithium (Li) in the Earth's crust, coupled with geographic concentration of its reserves, raise concerns about future supply chain constraints

Rishika Jakhar and Shrestha Ghosh contributed equally to this work.

[2–4] Sodium-ion batteries (SIBs) have recently emerged as promising complementary technology, offering advantages such as lower cost, material abundance, enhanced safety, and superior high- and low-temperature reliability compared to state-of-the-art LIBs [5–7] Integration of SIBs into the broader battery ecosystem is therefore crucial for meeting terawatt-hour-scale energy demands toward a decarbonized future [8].

However, the accessible energy density of SIBs remains substantially lower than that of commercial LIBs, which is largely imposed by the low capacity of the sodium-ion (Na-ion) cathode materials [9]. Among various cathode materials explored for SIBs, layered oxides have attracted particular attention due to their relatively higher capacities and lower costs [10, 11]. Layered Na oxides are categorized into P2 and O3 phases based on Na coordination (prismatic or octahedral) and oxygen layer stacking sequence (ABBA or ABCABC) [12]. Critically, P2-type structures offer superior Na^+ diffusion kinetics compared to O3-type structures due to the capability of direct hopping between prismatic sites for Na^+ ions through an open square channel [13]. Typically, P2-type materials exhibit better rate performance and cycle stability compared to O3-type materials. However, P2-type materials face several fundamental challenges that limit their practical implementation. First, the inherently lower Na content ($x \sim 0.67$) compared to O3 phases ($x \sim 1$) restricts the available Na^+ inventory and capacity [14]. Second, P2-type materials commonly undergo detrimental structural phase transitions to O2 (or intermediate OP4/Z phases) upon deep de-sodiation (>4.2 V), resulting in substantial volume changes and rapid capacity decay [15]. Third, P2-type materials often exhibit Na^+/vacancy ordering phenomena, where Na^+ ions and vacancies arrange into superstructures to minimize electrostatic repulsion. This ordering creates voltage plateaus in electrochemical profiles and can interact and impede Na^+ migration [16].

To enhance the accessible capacity, cycle stability, and rate performance of P2-type Na cathode materials, elemental substitution in the transition metal (TM) layer has emerged as an effective strategy. [17–23] Nonetheless, the single-element doping strategy present inherent limitations. For instance, Li^+ substitution alone can stabilize higher Na content in P2 type structures and modify the transition-metal redox chemistry but does not effectively control the reversibility of oxygen redox [21, 24], while Ti^{4+} doping enhances structural robustness but contributes little to redox activity [25]. Furthermore, higher doping levels often incur a capacity penalty due to the electrochemical inactivity of the dopant species. Hence, a synergistic design that integrates electronic and structural regulation is imperative to unlock the full potential of P2-type Na cathodes, enabling high-energy, high-power, and durable Na-ion batteries.

In this work, we employ a dual-substitution strategy combining Li^+ and Ti^{4+} doping to design high-Na content P2-type layered oxides with simultaneously enhanced capacity and electrochemical stability. Through comprehensive optimization and synchrotron X-ray characterizations, we demonstrate that Ti substitution effectively disrupts Na^+/vacancy and charge ordering at low state of charge (SoC) region ($\leq$ 4.2 V) and promotes oxygen participation at high SoC region (>4.2 V). Specifically, the partial substitution of Mn with Ti leads to an expansion of interlayer spacing, which is beneficial to the Na^+ diffusion kinetics thereby improving the rate performance. Moreover, the strong Ti—O increases the ionicity and charge density of oxygen, promoting reversible lattice-oxygen participation at high-voltage. This synergistic combination yields a balanced cationic–anionic redox mechanism that delivers higher reversible capacity, excellent rate capability, and robust structural integrity during extended high-voltage cycling. These findings establish design principles for high-performance P2-type cathodes, paving the way for next-generation Na cathode materials with high energy density and fast kinetics.

2 | Results and Discussion

We synthesized a series of high Na content, and Ti-doped P2 – $Na_{0.75}Li_{0.05}Ni_{0.3}Mn_{0.65}Ti_xO_2$ cathode materials via the solid-state synthesis. The materials have 5% Li substituted in the transition metal layer to increase the Na content in this compound, from 0.67 to 0.75. The crystal structures of $Na_{0.75}Li_{0.05}Ni_{0.3}Mn_{0.65}O_2$ (NaLNMT0) and $Na_{0.75}Li_{0.05}Ni_{0.3}Mn_{0.59}Ti_{0.06}O_2$ (NaLNMT6) were characterized by X-ray Diffraction. For comparison, two other Ti-doped candidates—$Na_{0.75}Li_{0.05}Ni_{0.3}Mn_{0.62}Ti_{0.03}O_2$ (NaLNMT3) and $Na_{0.75}Li_{0.05}Ni_{0.3}Mn_{0.55}Ti_{0.1}O_2$ (NaLNMT10) were also synthesized. In this design, Ni^{2+} serves as the primary redox center, leveraging the reversible $Ni^{2+}/Ni^{3+}/Ni^{4+}$ redox couple, while Li^+ incorporation enables higher Na content (0.75) while maintaining charge neutrality. ICP–MS analysis (Table S1) confirms that the Li-free, Ti-containing reference composition $Na_{0.6}Ni_{0.3}Mn_{0.64}Ti_{0.06}O_2$ (NaNMT6) contains a significantly lower Na content than Li-substituted NaLNMT compositions, supporting the role of Li incorporation in enabling high Na-content P2 type structures. The average cationic potential calculations shown in Figure 1a for the designed layered sodium transition metal oxides confirm that high Na content and Ti substitution are within the thermodynamic stability of the P2-type phase.

Synchrotron XRD patterns coupled with Rietveld refinement confirm the phase purity and crystal structure for NaLNMT0 and NaLNMT6 (Figure 1b,c). All diffraction peaks index to the hexagonal space group $P6_3/mmc$, confirming the P2-type layered structure. Notably, Ti substitution induces systematic lattice expansion: the *a*-axis lattice parameter increases from 2.887 Å (NaLNMT0) to 2.893 Å (NaLNMT6), and the *c*-axis lattice parameter increases from 11.072 Å to 11.096 Å (Tables S2–S5), thus expanding the interlayer spacing and potentially reducing the Na^+ migration barrier during electrochemical cycling. However, the c-lattice parameter does not evolve uniformly, especially for the endmember NaLNMT10, likely due to cubic impurity phase NiO as observed in XRD (Figure S1).

SEM analysis shown for NaLNMT6 in Figure 1d and NaLNMT0 (Figure S2) reveals well-defined platelet-like particles with lateral dimensions of 5–8 μm, which is characteristic of solid-state synthesized layered oxides. HAADF-STEM imaging of NaLNMT6 along the [100] zone axis, shown in Figure 1e shows the layered structure with a measured interlayer d-spacing of $\sim$ 0.586 nm, which aligns with the crystallographic interslab distance obtained from Rietveld refinement. EDS elemental mapping shown in Figure 1f for NaLNMT6 demonstrates uniform distribution of Na, Ni, Mn, Ti, and O throughout the particles with no evidence of elemental segregation or secondary phases.

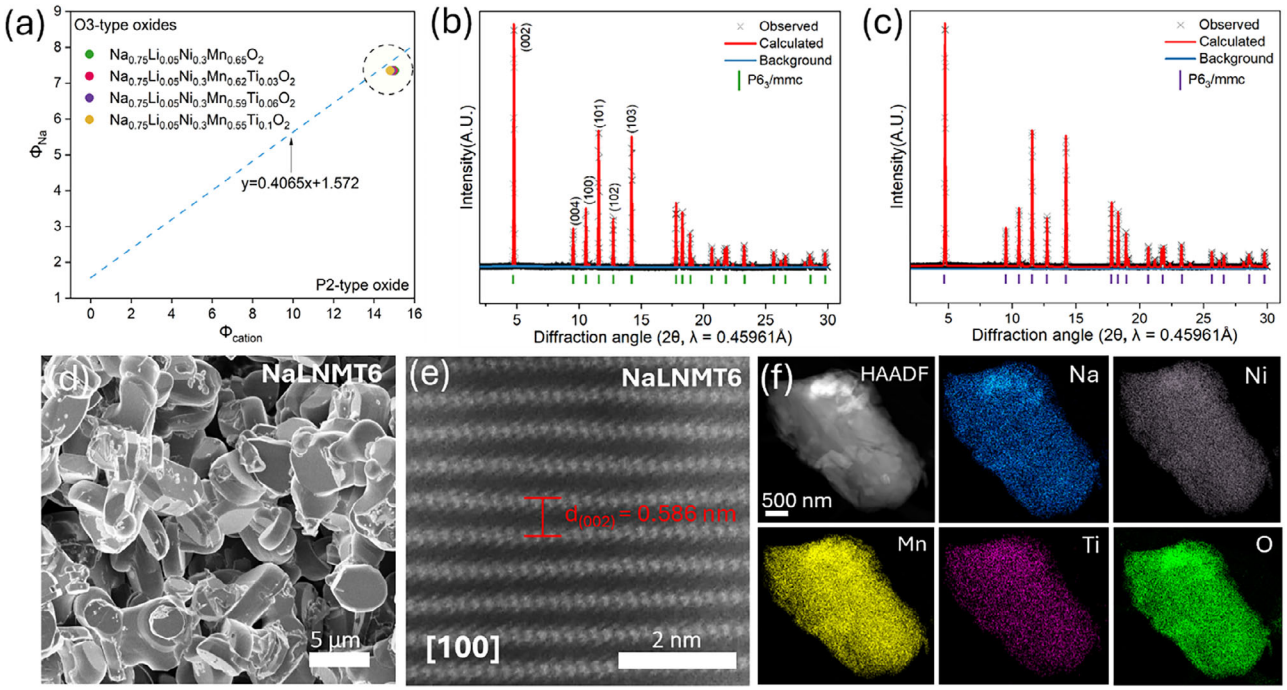

FIGURE 1 | (a) Cationic potential of the different synthesized P2-type materials considering the Na content, oxidation sate and addition of Ti in the TM layer. (b and c) Synchrotron XRD and Rietvald refinement plot of NaLNMT0 and NaLNMT6 materials prepared by solid state synthesis. (d) SEM images, (e) HAADF-STEM image along [100] zone axis, and (f) energy-dispersive X-ray spectroscopy mapping of P2-NaLNMT6.

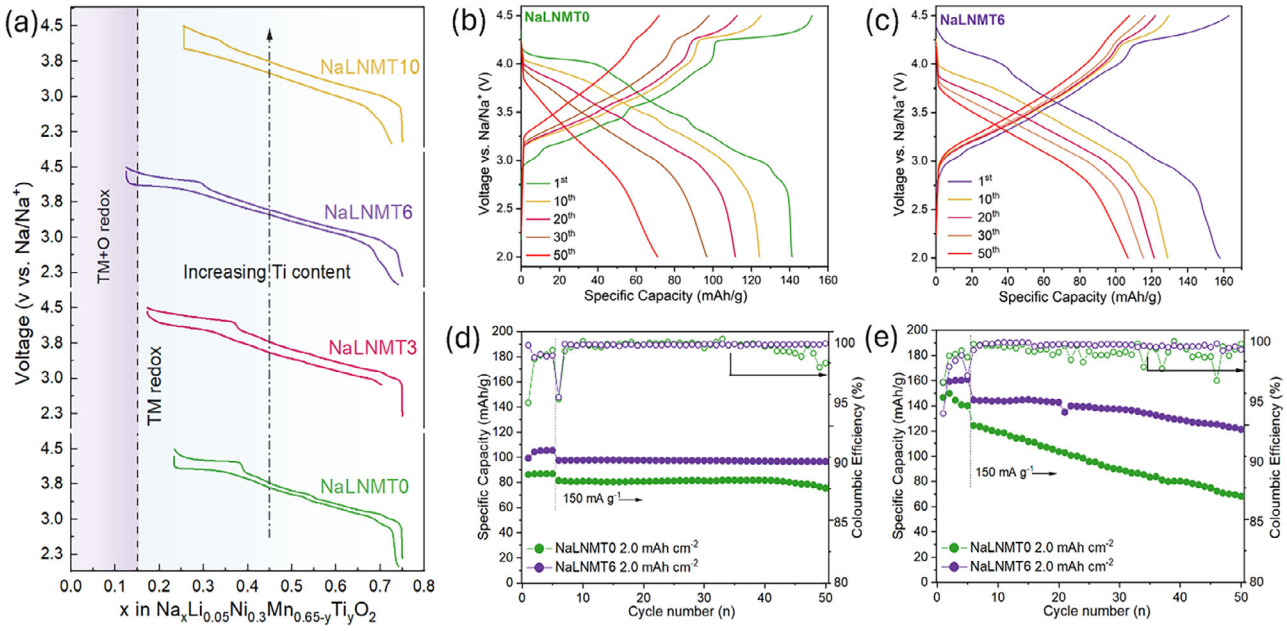

FIGURE 2 | (a) Voltage profiles of the P2 $Na_{0.75}Li_{0.05}Ni_{0.3}Mn_{0.65-x}Ti_xO_2$ materials versus metallic sodium cycled between 2.0–4.5 V vs Na^+/Na^0 at 15 mA g^{-1}. Typical charge/discharge profiles of (b) NaLNMT0 and (c) NaLNMT6 between 2.0 and 4.5 V during 10^{th}, 20^{th}, 30^{th} and 50^{th} cycle at 150 mA g^{-1}. Long-term cycling tests of NaLNMT0 and NaLNMT6 operated between (d) 2.0–4.2 V and (e) 2.0–4.5 V with areal loading of 2.0 mAh cm^{-2} at 150 mA g^{-1}. Five formation cycles at 7.5 mA g^{-1} were conducted before the cycling test.

The electrochemical performance characteristics of all synthesized materials were first evaluated in Na half-cells with an areal loading of 0.5 mAh cm^{-2} cycled between 2.0–4.5 V at a 15 mA g^{-1} at 25°C (Figure 2a; Figure S3). Increasing the Ti substitution from 0% to 3% to 6% progressively enhances the reversible capacity, with the NaLNMT6 composition exhibiting greater sodium extraction compared to the Ti-free NaLNMT0. Compared with Li/Ti co-doped NaLNMT, the Li-free NaNMT6 exhibits lower reversible capacity and inferior long-term cycling stability (FigureS4), indicating that Ti substitution alone is

insufficient to achieve both high capacity and long-term structural stability.

NaLNMT0 delivers a reversible capacity of 135 mA g^{-1}, corresponding to the extraction of approximately 0.52 Na per formula unit. This is below the theoretical capacity based on the Ni^{2+}/Ni^{4+} two-electron redox process (0.60 Na per formula unit, 156 mA g^{-1}), indicating that the full Ni redox capacity is not achieved at the 4.5 V voltage cutoff. With Ti^{4+} substitution, NaLNMT6 exhibits a higher reversible capacity of 163 mA g^{-1}, equivalent to the extraction of approximately 0.62 Na per formula unit. This exceeds the theoretical capacity expected from Ni^{2+}/Ni^{4+} redox alone suggesting the involvement of additional charge compensation mechanisms beyond conventional TM redox, which will be discussed later. Meanwhile, as shown in Figure 2b,c the charge-discharge profile of NaLNMT6 displays a smooth voltage profile compared to NaLNMT0 and higher cycling stability when cycled up to 4.5 V. The differential capacity analysis (dQ/dV) and cyclic voltammetry (Figures S5 and S6) demonstrate that Ti^{4+} substitution leads to broader, less intense redox peaks, indicating a transition toward solid-solution-type behavior during Na (de)intercalation and suppressing the formation of Na^+/vacancy-ordered superstructures [18]. However, the relationship between observed progressive capacity increase and the gradual decrease in Na^+/vacancy ordering with Ti substitution from 0% to 6% is not fully understood and warrants further investigation to elucidate the underlying mechanism. The remainder of this study focuses on these two compositions to systematically investigate how Ti incorporation modifies the charge compensation mechanisms in these Li-containing P2-type cathode materials.

To demonstrate the practical applicability of these materials, we fabricated high-mass-loading electrodes (~ 2 mAh cm^{-2}) and evaluated their cycling performance, shown in Figure 2d,e. The cells were initially cycled at 7.5 mA g^{-1} to facilitate the activation of redox processes throughout the electrode bulk, followed by galvanostatic cycling at 150 mA g^{-1}. Both NaLNMT0 and NaLNMT6 exhibited remarkable cycling stability under these conditions, retaining their respective capacity trends, with NaLNMT6 maintaining its superior capacity even with higher mass loading electrodes. As shown in Figure 2d, when tested up to 4.2 V both NaLNMT0 and NaLNMT6 demonstrate exceptional cycling stability with capacity retentions of 93% (NaLNMT0) and 98% (NaLNMT6) after 50 cycles. As shown in Figure 2e, when cycling over an extended voltage window up to 4.5 V, NaLNMT6 retains 76% of its capacity after 50 cycles compared with only 48% for NaLNMT0, highlighting the synergistic stabilization by Li and Ti during high voltage operation.

To evaluate the practical relevance of the Li/Ti co-doping strategy, Na-ion full cells were assembled using hard carbon (HC) anodes paired with NaLNMT0 and NaLNMT6 cathodes (Figure S7). Given the substantial initial irreversible capacity associated with HC, the anodes were pre-sodiated by cycling in half cells prior to full-cell assembly to mitigate Na inventory loss. With pre-sodiated HC, the full cells exhibit electrochemical behavior closely resembling their respective half-cell behavior. At different current densities (i.e., 15 and 30 mA g^{-1}), NaLNMT6 shows higher capacity with better cycling stability compared to NaLNMT0, demonstrating the practical improvement of Na cathode with Li/Ti co-doping. Future work can be focused on improving hard carbon stability and kinetics as well as Na inventory balance, to further boost full-cell performance.

These results collectively affirm that strategic Ti substitution in high-Na-content layered oxides effectively suppresses phase transitions, enhances reversibility, and activates additional redox contributions, positioning NaLNMT6 as a highly promising cathode for next-generation sodium-ion batteries.

To elucidate charge-compensation in NaLNMT0 and NaLNMT6 during sodiation and de-sodiation, we performed ex situ soft and hard X-ray absorption spectroscopy (XAS) to track the evolution of transition-metal and oxygen states at selected state-of-charge points. During charging, the Ni K-edge XANES (Figure 3a,b) and the half-edge energy ($E_{0.5}$, inset; half-height method) show the expected increase in $E_{0.5}$ upon charge (Na^+ extraction) and decrease upon discharge (Na^+ insertion), indicating the regular cationic redox behavior [26]. For both compositions, $E_{0.5}$ rises monotonically from pristine to 4.5 V, evidencing oxidation of Ni^{2+} to higher valence states. During discharge (Figure S8), the Ni ions are reduced back to Ni^{2+}, indicating good reversibility of Ni redox. Notably, NaLNMT6 displays higher $E_{0.5}$ already at 4.0 and 4.2 V than NaLNMT0. This indicates that Ni in the Ti-doped material attains higher oxidation states at lower potentials and thus Ti can promote faster Ni redox kinetics. This trend is corroborated by Ni K-edge EXAFS as shown in Figure 3c (Figure S9 and Tables S6 and S7), the first-shell peak yields shorter Ni—O distances at 4.2 V for NaLNMT6 (1.92 Å) than for NaLNMT0 (2.01 Å), consistent with higher Ni valence in NaLNMT6. In contrast, the Mn ions show only a minor participation in the electrochemical charge transfer reaction and remain essentially all Mn^{4+} (Figure S10). Prior studies on P2-type layered oxides have shown that Li substitution within the transition-metal layer can increase Ni redox participation and, in some cases, temper oxygen-redox activity [24, 27] In our Li/Ti-modified NaLNMT6, the enhanced Ni participation is evident from XANES/EXAFS, yet its higher capacity relative to NaLNMT0 cannot be rationalized by cationic redox alone as discussed previously in Figure 2a. Taken together, these results indicate that local TM-layer chemistry (Li/Ti substitution and Ti—O bonding) modulates Ni redox thermodynamics and TM—O covalency, while additional charge compensation, likely involving lattice-oxygen redox, can contribute to the excess capacity observed in NaLNMT6.

To probe the evolution of Oxygen states during electrochemical cycling, O K-edge soft X-ray absorption spectroscopy (sXAS) was conducted in total fluorescence yield (TFY) mode, providing information on the bulk electronic structure. The pre-edge region below 535 eV corresponds to O(1s) → O(2p)/TM(3d) hybridized transitions, while the broader features above 535 eV arise from O(1s) →O(2p)/TM(4sp) hybridized states. The pre-edge can be deconvoluted into t_{2g} (~529.7 eV) and e_g (~531.8 eV) components, reflecting crystal-field splitting under octahedral coordination [27, 28]. Although TM—O hybridization dominates the O K-edge response and thus the spectra alone cannot unambiguously confirm oxygen redox activity, the evolution of the pre-edge region provides important qualitative insight into Oxygen participation. Notably, as shown in Figure 3d,e while the overall line shape of NaLNMT0 remains unchanged upon charging, NaLNMT6

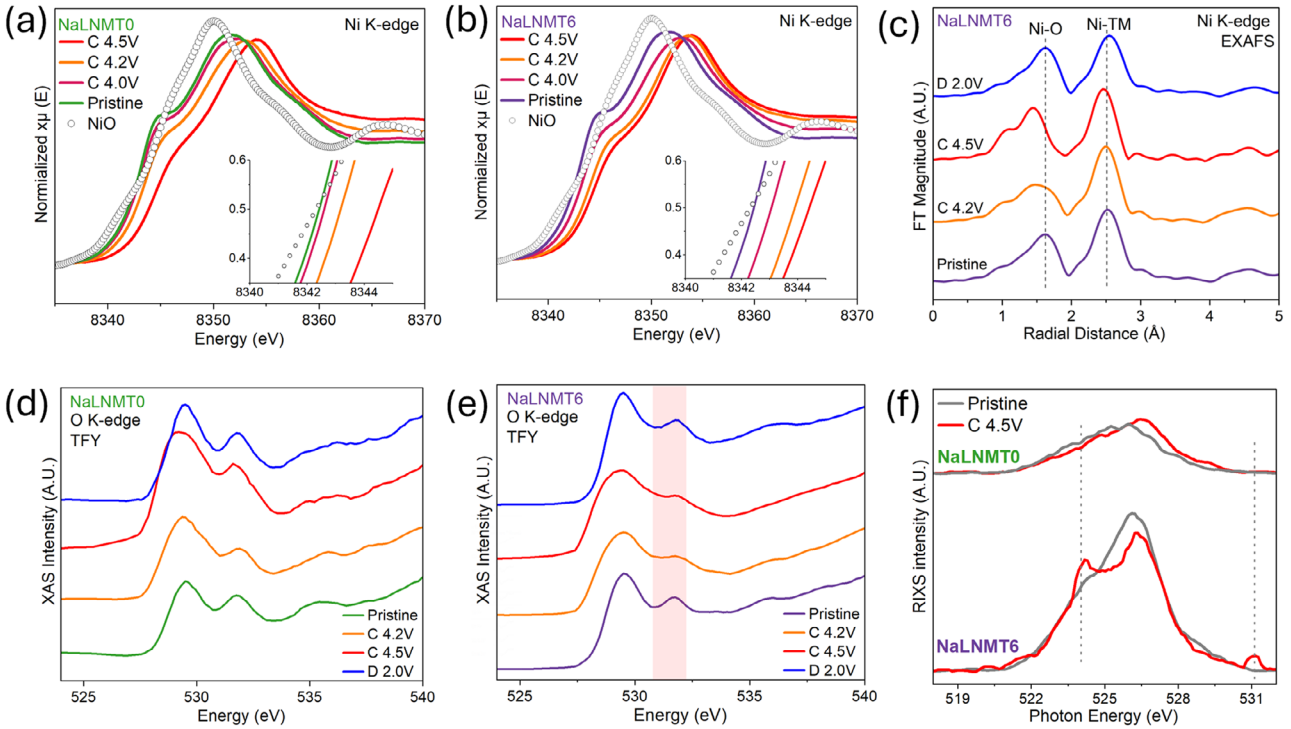

FIGURE 3 | Ex situ Ni K-edge XANES (a) NaLNMT0 and (b) NaLNMT6. The inset is the zoomed-in region around the half-edge. (c) Ex situ Ni-K edge EXAFS of NaLNMT6. TFY O K-edge XAS at various states of charge (d) NaLNMT0 and (e) NaLNMT6. (f) RIXS spectra of pristine and charged state (4.5 V) NaLNMT0 and NaLNMT6 collected at a 531.6 eV excitation energy. The prefixes "C" and "D" indicate the charged and discharged state, respectively.

exhibits a clear attenuation of the shoulder feature between 531 and 532 eV, particularly from 4.2 V to 4.5 V. This loss of intensity signifies the emergence of a new oxidized oxygen species at high voltages, consistent with partial participation of lattice oxygen in charge compensation [27, 29] The onset of this spectral evolution above 4.2 V aligns with the enhanced reversible capacity observed in NaLNMT6, supporting the coexistence of cationic and anionic redox processes in the Ti- and Li-doped system.

Mechanistically, the oxygen oxidation observed in NaLNMT6 does not follow a reductive coupling mechanism, wherein electrons from oxidized oxygen species are transferred to neighboring transition metals [30, 31]. This inference is supported by the Ni K-edge hard XAS results, which show no measurable reduction of the transition-metal species at high voltages.

To reveal the intrinsic lattice-oxygen redox activity, high-efficiency mapping resonant inelastic X-ray scattering (mRIXS) was employed, a technique now widely recognized as the most sensitive probe for detecting unreleased oxidized oxygen species in battery electrodes. A distinct emission feature centered near 523.7 eV serves as the spectroscopic fingerprint of oxidized lattice oxygen [19]. This characteristic feature has been firmly established across both Li- and Na-based layered oxides as a reliable indicator of lattice-oxygen redox activity [19, 32]

O K-edge RIXS measurements were performed on ex situ cathodes charged to 4.5 V to examine the nature of these oxidized oxygen states. Reversible oxygen redox activity in layered oxides is often linked to subtle changes in local oxygen coordination and the partial oxidation of lattice oxygen species. In NaLNMT6, the mRIXS maps (Figure S11) show no pronounced high-intensity feature typically associated with molecular-like O—O interactions. Instead, a localized spot in the mRIXS map corresponds to the energy region captured in the RIXS line scan (Figure 3f; Figure S12), which highlights the emergence of an inelastic shoulder near 523.7 eV emission energy at the charged state. This shoulder reflects the oxidation of lattice oxygen and confirms the presence of an oxygen redox process in NaLNMT6 [33, 34]

To further assess whether the activated oxygen redox is accompanied by irreversible oxygen release or oxygen-driven parasitic reactions, differential electrochemical mass spectrometry (DEMS) measurements were conducted during the first charge (Figure S13). While NaLNMT0 exhibits negligible gas evolution over the investigated voltage range, NaLNMT6 shows a pronounced increase in CO_2 evolution at high voltages approaching 4.5 V. Direct O_2 evolution is not dominant under these conditions. The enhanced CO_2 generation is therefore attributed to the presence of highly reactive oxidized oxygen species that can chemically interact with the carbonate electrolyte, rather than to direct lattice-oxygen release as molecular O_2 [35–39] These DEMS results are consistent with the mRIXS observations, indicating that oxygen redox in NaLNMT6 is primarily due as lattice-oxygen oxidation, though it is accompanied by interfacial side reactions at high-voltages.

In the Ti-doped analogues, while Ti^{4+} remains electrochemically inactive within the 2.0–4.5 V window, it primarily functions as a structural and electronic stabilizer rather than a

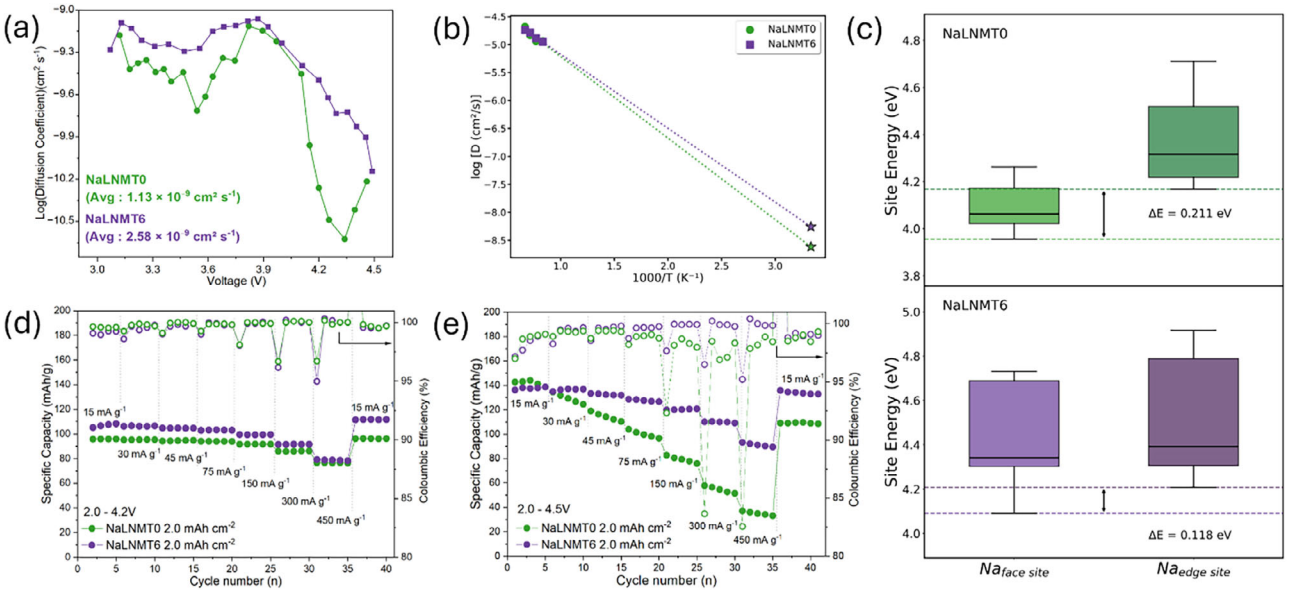

FIGURE 4 | (a) Calculated Na^+ ion diffusion coefficients from GITT of NaLNMT0 and NaLNMT6 samples as a function of voltage during Na extraction processes. (b) Arrhenius plot of Na^+ diffusion coefficients obtained from ML-MD calculations (c) Calculated energy difference per Na atom between the Na_{edge} and Na_{face} site for NaLNMT0 and NaLNMT6. Rate performance comparison of NaLNMT0 and NaLNMT6 cathodes with areal loading of 2.0 mAh cm^{-2} from 15 to 450 mA g^{-1} with voltage range of (d) 2.0–4.2 V and (e) 2.0–4.5 V. Five formation cycles were conducted at 15 mA g^{-1} before the rate test.

redox-active center. Its relatively large ionic radius and strong Ti—O bond (~662 kJ mol^{-1}) modulate the covalency of adjacent TM—O bonds [40]. Owing to its highly ionic character, Ti^{4+} reduces TM—O covalency in neighboring sites, localizing greater electron density on oxygen and subtly tuning the electronic landscape of the TM layer. The presence of Li further complements this effect by enabling stabilization of Na-rich P2-type structures and facilitating deeper de-sodiation. The highly ionic Li—O bond can further increase the electron density around oxygen, facilitating charge localization. While Li—O—Na configurations are known to create the electronic conditions for oxygen participation, the present results indicate that Ti incorporation is essential to activate oxygen redox electrochemically at high voltages [41, 42] Taken together, Li and Ti act synergistically: Li stabilizes Na-rich composition, while Ti enhances high-voltage structural robustness and moderates oxygen activity, enabling oxygen redox in NaLNMT6 [43, 44]

To further understand the capacity increase mechanism after Ti substitution, the Na^+ transport kinetics were compared between the two materials. Galvanostatic intermittent titration technique (GITT) measurements were conducted for both NaLNMT0 and NaLNMT6. As shown in Figure 4a (Figure S14), the apparent Na^+ diffusion coefficient (D_{Na^+}) varies with voltage during cycling between 2.0–4.5 V. NaLNMT6 exhibits a consistently higher D_{Na^+} across the potential range, averaging 2.58×10^{-9} cm^2 s^{-1}, nearly twice that of NaLNMT0 (1.13×10^{-9} cm^2 s^{-1}). This enhancement reflects the beneficial effect of Ti incorporation on Na-ion mobility. The GITT-derived Na^+ diffusion coefficient of NaLNMT0 exhibits a pronounced local minimum near ~4.2 V, characteristic of layered Na cathodes undergoing high-voltage structural evolution to OP4/O2-type phase, whereas NaLNMT6 maintains a more stable diffusion profile throughout charge and discharge [45–47]

This improvement is linked to the observed expansion of the *c*-lattice parameter upon Ti doping, which reduces Na^+ migration barriers by widening the diffusion channels and weakening Na—O electrostatic interactions. From the mean-square-displacement (MSD) analysis, the diffusion coefficient (D_{Na^+}) was extracted by fitting the slope of the MSD–time curves. The diffusivity values derived for NaLNMT0 (3.34×10^{-9} cm^2 s^{-1}) and NaLNMT6 (5.59×10^{-9} cm^2 s^{-1}) are in good agreement with the experimental results. The Arrhenius plots derived from Molecular Dynamics (MD) calculations done with Machine Learning (ML) interatomic potentials (Figure 4b) yield activation energies (E_a) of 261 meV for NaLNMT6 and 279 meV for NaLNMT0, confirming a lower migration barrier and faster ionic transport in the Ti-doped material.

In the P2-type layered structure, sodium ions occupy two distinct prismatic sites: the edge-sharing site (Na_{edge}) and the face-sharing site (Na_{face}), which differ in their local coordination environment with the adjacent transition-metal layers. Density functional theory (DFT) calculations (Figure 4c) reveal that Li/Ni/Mn/Ti cation mixing significantly reduces the site-energy difference between Na_{edge} and Na_{face} sites. The calculated site energy difference for the most stable Na_{face} site and Na_{edge} site is 221.4 meV for NaLNMT0 and 117.6 meV for NaLNMT6.

This energetic homogenization suppresses Na^+/vacancy ordering and thereby mitigates the formation of strongly ordered intermediate phases. As a result, Ti substitution promotes continuous solid-solution-type Na^+ de-intercalation behavior and thus stabilizes Na-ion diffusion pathways. Rate capability tests were further performed in the voltage ranges of 2.0–4.2 V and 2.0–4.5 V at rates from 15 mA g^{-1} to 450 mA g^{-1} (Figure 4d,e). Within the 4.2 V window, both materials exhibit excellent rate performance and cycling stability. The slight capacity drop of NaLNMT6 at

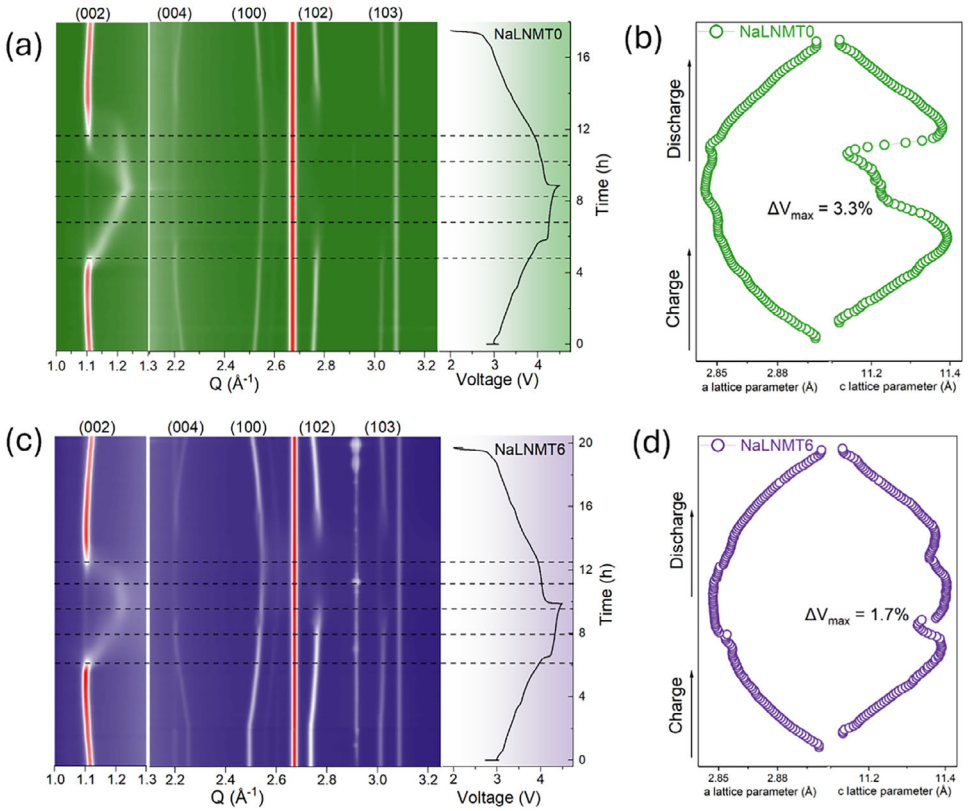

FIGURE 5 | 2D contour plots of in situ XRD for the structural evolution of (a) NaLNMT0 (c) and NaLNMT6 during the initial cycle at 15 mA g^{-1} in the voltage range of 2.0–4.5 V. The evolution of c-axis and a-axis lattice parameters obtained from Rietveld refinements for (b) NaLNMT0 and (d) NaLNMT6.

higher rates is attributed to the slower kinetics of the oxygen redox activity at 4.2 V. However, in the extended 4.5 V window, NaLNMT0 suffers a pronounced capacity decay, consistent with the diffusion drop observed near 4.2 V, whereas NaLNMT6 exhibits superior rate performance and structural stability. Although Li co-substitution in both compositions mitigates P2→OP4 phase transitions, Ti doping further strengthens the structural robustness and improves Na-ion transport, collectively enabling fast and reversible electrochemical kinetics in NaLNMT6.

Given the marked differences in Na^+ diffusion kinetics and rate performance, it is essential to understand how Ti substitution influences the structural evolution of the layered framework during (de)sodiation. To this end, in situ X-ray Diffraction (XRD) measurements were carried out for both NaLNMT0 and NaLNMT6 at different C rates of 15 and 75 mA g^{-1}. The results for 15 mA g^{-1} are shown in Figure 5a,c and Figure S15.

Upon initial charging to 4.2 V, both compositions exhibit systematic peak shifts corresponding to an increase in the interlayer spacing (*c*-lattice parameter) and a decrease in the in-plane TM–TM distance (*a*-lattice parameter) (Figure 5b,d). The expansion of the *c* parameter arises from reduced electrostatic screening between adjacent negatively charged oxygen layers as Na^+ ions are extracted, while contraction of the '*a*' parameter results from shortening of TM—O bonds upon oxidation of transition metals. During charging, the (002) and (004) reflections move to lower angles, signifying *c*-axis expansion due to increased inter-slab repulsion, whereas the (100) and (102) reflections shift to higher angles, indicating *ab*-plane contraction linked to Ni^{2+} / Ni^{4+} oxidation.

At voltages above 4.2 V, both samples show a plateau in the electrochemical curve, characteristic of a two-phase transition. In NaLNMT0, the (002) reflection abruptly shifts to higher angles at high voltages, consistent with the development of O-type stacking faults and OP4/O2-type intergrowth domains within the P2 framework [25, 33, 48–50] This P2 → OP4/O2-type intergrowth evolution originates from gliding of the TM—O slabs from ABBA toward ABAC stacking and induces a maximum volume change of approximately 3.3% in NaLNMT0. In contrast, Ti-substituted NaLNMT6 follows similar peak-shift trends but with more mitigated structural distortion. At high voltages, the shift of the (002) reflection is strongly suppressed, and the growth of the OP4 phase region is markedly narrowed. The overall volume change is limited to 1.7%, nearly half that of NaLNMT0. Although Li incorporation is known to moderate P2 to OP4 to O2-type evolution, these results show that Li alone (as in NaLNMT0) cannot prevent structural collapse above 4.0 V; Ti co-substitution is required to maintain lattice stability across the extended 4.5 V window. Ex situ XRD at 4.5 V (Figure S16) is consistent with in situ measurements with NaLNMT0 showing a distinct right shift of the (002) reflection at 4.5 V, whereas NaLNMT6 exhibits peak broadening with minimal peak displacement, indicating suppressed P2 to OP4 transition.

At the higher C rate of 75 mA g^{-1} (Figures S17 and S18), the difference in structural reversibility becomes even more

evident. NaLNMT0 fails to fully recover its initial structure upon discharge—the (002) reflection does not return to the pristine position, and progressive peak broadening indicates accumulating disorder. Conversely, NaLNMT6 exhibits nearly complete structural reversibility. Ex situ XRD post cycling further confirms the reduced crystal structure degradation of NaLNMT6 relative to NaLNMT0 as shown by the stronger intensity attenuation in NaLNMT0 (Figure S19).

The evolution of the *c*-lattice parameter (Figure 5b,d) further illustrates this contrast. NaLNMT0 undergoes a sharp *c*-axis contraction of ~3% upon charging to 4.5 V, accompanied by a clear discontinuity at high voltage that signifies the P2→OP4/O2 type transition. In comparison, NaLNMT6 displays a modest *c*-axis variation of only ~1%, despite extracting a larger quantity of Na^+ than NaLNMT0. While conventional P2-type oxides typically undergo layer gliding when Na content drops below x ~ 0.33, NaLNMT6 preserves the P2 framework even under deep (de)sodiation states. Ti substitution, therefore, can enhance the thermodynamic stability of the P2 phase and minimize structural strain.

Two primary factors account for the suppressed phase transition and small volume change observed in both compositions. First, Li doping stabilizes higher Na content within the P2 lattice, and the remaining Na^+ effectively screens electrostatic repulsion between adjacent TM—O slabs. Retaining more Na^+ during charging mitigates the driving force for layer gliding and preserves structural order. Second, Ti substitution strengthens TM—O bonding, as Ti—O (~ 662 kJ mol^{-1}) is significantly stronger than Mn—O (~ 402 kJ mol^{-1}) or Ni—O (~ 392 kJ mol^{-1}) [40, 44]. The stronger, more ionic Ti—O bonds can alleviate anisotropic distortion of the TM—O framework, limiting lattice expansion and contraction during cycling. Together, these effects enable NaLNMT6 to achieve higher capacity and structural stability.

3 | Conclusions

In this work, we employ a comprehensive experimental and spectroscopic approach to elucidate how rational cation substitution can couple electronic modulation with structural stabilization in high-Na P2-type layered oxides. Using electrochemical measurements, in situ XRD, and hard and soft X-ray spectroscopies, we reveal that Li and Ti co-doping enhances sodium storage reversibility and structural robustness. Ti substitution accelerates Na^+ diffusion, mitigates phase transitions, and promotes lattice oxygen redox with its strong Ti—O bonding. Whereas the coexistence of Li^+ in the TM layer allows for more Na to be introduced in a P2-type structure promoting higher Na retention during charging, and mitigating layer gliding. Combined spectroscopic evidence, including soft XAS and RIXS analyses, confirms the activation of reversible oxygen redox. Together, these effects establish a clear correlation between transition-metal–oxygen covalency, lattice stability, and oxygen redox reversibility. The cooperative Li–Ti dual-doping strategy thus provides a guiding principle for designing high-energy, long-life sodium-ion cathodes through the synergistic tuning of cationic and anionic redox processes.

4 | Experimental Section

4.1 | Synthesis

All samples were synthesized via a solid-state reaction. First, stoichiometric amounts of NiO (99.99%, Sigma-Aldrich), MnO_2 (≥99%, Sigma-Aldrich), TiO_2 (99.8%, Sigma-Aldrich), 5% excess of Li_2CO_3 (99%, Alfa Aesar), and 10% excess of Na_2CO_3 (≥99.5%, Sigma-Aldrich) were mixed and ground in an agate mortar for 15 min. The powders were then ball milled (Fritsch Pulverisette 7) at 400 rpm for 4 h (alternating between 15 min of effective milling and 15 min of rest). The mixed powders were calcined at 950°C for 24 h in a muffle furnace (Carbolite Gero, CWF-B 1200). The resulting powders were transferred to an Argon-filled glove box antechamber while maintaining a temperature of 150°C to avoid exposure to moisture.

4.2 | Electrochemical Measurements

Electrodes were prepared by mixing each of the layered oxides with conductive additive, Super P (MTI corp), and binder polyvinylidene fluoride (PVdF) in N-methyl pyrrolidone (NMP) in a ratio of 90:5:5 (active material:Super P:PVdF) to form a well-homogenized slurry. The slurry was casted using a doctor blade method on a carbon-coated Aluminum foil and was then dried in a vacuum oven overnight at 120°C. The electrodes were transferred to an Argon-filled glove box (Vigor, H_2O and O_2 content <0.1 ppm) for half-cell assembly. The dried electrodes with areal loading ~0.5 mAh cm^{-2} were used for half cell testing using Na metal as the anode and Whatman GF/F borosilicate glass fiber as the separator. The electrolyte used for both half and full cell study was 1 M $NaPF_6$ in Propylene Carbonate (PC) mixed with 6wt% of Fluoroethylene Carbonate (FEC) as an additive, and the electrolyte volume added was 80 µl. All cells were rested for 6 h followed by 2 formation cycles in 2.0–4.5 V at 15 mA g^{-1}, for activation of redox processes in both bulk and surface of the material. For electrodes with a high areal loading of 2 mAh cm^{-2}, the electrolyte volume was increased to 150 µl followed by 5 formation cycles at 7.5 mA g^{-1}

For the full cell studies, a hard carbon anode was prepared by mixing hard carbon from Kuraray with conductive additive and binder polyvinylidene fluoride (PVdF)) in a ratio of 90:5:5 and coated on Al foil to be used as the negative electrode in CR2032 coin-type Na-ion full cells. The negative to positive material (N/P) ratio of 1.1. The full cells were cycled between the voltage window of 0.7–4.19 V.

For the GITT tests, the batteries were charged at 15 mAh g^{-1} for 10 min, followed by open-circuit relaxation for 4 h. The diffusion coefficient was calculated as [51]:

$$D = \frac{4}{\pi \tau} \left(\frac{m_B V_M}{M_B S} \right)^2 \left(\frac{\Delta E_s}{\Delta E_t} \right)^2$$

where τ is the duration of current pulse (s), m_B is the mass of the active material (g), V_M is the molar volume of the material (cm^3 mol^{-1}), M_B is the molar mass of the material (g mol^{-1}) S is the surface area of the electrode (cm^2), ΔE_s is the steady state voltage change and ΔE_t is the total voltage change.

DEMS measurements were applied to detect and identify gas evolution of different cathode materials during the first charge/discharge. The DEMS was built based on a commercial mass spectrometer (HPR-40, Hiden Analytical). A home-made cell with electrolyte consisting of 1 M $NaPF_6$ in Propylene Carbonate (PC) mixed with 6wt% of Fluoroethylene Carbonate (FEC) as an additive was used for in situ measurements. To enhance measurement precision, an intermittent gas sampling was implemented, and a controlled vacuum was applied to ensure complete collection of the evolved gases. The released gases were accumulated inside the cell for 60 min prior to being introduced into the mass spectrometer for detection. The cells were then cycled at a current rate of 15 mA g^{-1} between 2.0 and 4.5 V versus Na^+/Na, using high-loading electrodes (2 mAh cm^{-2}) as positive electrodes to ensure better accuracy from machines.

4.3 | Structural Characterization

SEM imaging was performed using a Thermo Scientific Aquilos Cryo-focused ion beam (FIB)/SEM. Powders were prepared inside an argon-filled glovebox and transferred using an air-tight transfer arm. Atomic-resolution images of the NaLNMT0 and NaLNMT6 cathodes were acquired using an aberration-corrected Thermo Fisher Scientific Spectra Ultra X (Iliad) scanning transmission electron microscope operated at 300 kV in HAADF mode. The imaging was done at room temperature, and ImageJ software was used for post-processing. Elemental compositions were determined with inductively coupled plasma—mass spectrometry (ICP-MS) using Thermo iCAP RQ ICP-MS. Standards for the calibration curve were prepared using a stock multi-element standard containing each element (Inorganic Ventures). The laboratory-based XRD was conducted using a Rigaku SmartLab diffractometer using Cu Kα radiation (λ = 1.54 Å) over a 2θ range of 5–90°. X-ray Diffraction characterization was conducted at the 17 BM beamline of the Advanced Photon Source (λ = 0.45961 Å).

4.4 | In Situ X-Ray Diffraction Measurements

In situ X-ray Diffraction characterization during the charge-discharge process was conducted at the 17 BM beamline of the Advanced Photon Source (λ = 0.2526 Å). The tested 2032-type coin cell cases were modified with holes on both the cathode and anode caps and sealed with Kapton tape. The voltage profiles obtained during in situ XRD are fully consistent with conventional electrochemical measurements, with minor deviations attributable to the in situ cell configuration (Figure S20). Electrochemical cycling was performed using a MACCOR battery testing system. A standard reference material CeO_2, was measured to obtain the instrument parameters for sample data analysis. Rietveld refinements were processed using the sequential refinement function in the GSAS-II software package.

4.5 | Hard XAS Measurements

All the XAS spectra were collected under room temperature with the transmission signals. To prepare the samples for Hard XAS (hXAS) measurements, once the desired SoC was achieved, the coin cells were disassembled in the glovebox carefully (prevent short-circuiting) and as soon as possible (to minimize self-discharge under open circuit). The positive electrode powders were rinsed thoroughly three times with anhydrous dimethyl carbonate (DMC) to eliminate electrolyte residues and soluble surface species. DMC was evaporated by leaving the samples in a vacuum (using the glovebox antechamber) for at least 2 h. The ex situ cathode samples were sandwiched between a Kapton tape in an argon-filled glove box and then transferred from the glove box into a transport container and then into an X-ray absorption antechamber through an argon environment to minimize the potential exposure to air. The Ni and Mn K-edge XAS measurements were performed at 7-BM-B beamline of the National Synchrotron Light Source II (NSLS-II) at Brookhaven National Laboratory. The obtained data were normalized and analyzed using Athena software. The EXAFS fittings were performed in Artemis software (Figures S21 and S22)

4.6 | Soft XAS and RIXS Measurements

The O *K*-edge soft XAS (sXAS) and O K-edge RIXS spectra were collected by the iRIXS end station at beamline 8.0.1 in Advanced Light Source, Lawrence Berkeley National Laboratory. A custom-built transfer kit was employed to transport the samples from the Ar-filled glovebox to the measurement chamber, ensuring complete protection from air exposure. The RIXS spectra were continuously scanned through the O-*K* pre-edge region with the excitation energy step size of 0.2 eV. The collected spectra were fabricated to 2D RIXS maps as functions of emission and excitation energies. The sXAS data shown in this work are measured in both total fluorescence yield (TFY) and total electron yield (TEY) modes. We use the TFY data for detailed analysis in this work due to its bulk sensitivity. All spectra have been normalized to the photon flux.

4.7 | Computational Methods

All density functional theory (DFT) calculations were performed using the Vienna Ab initio Simulation Package (VASP) within the projector augmented-wave (PAW) formalism [52, 53]. The Perdew-Burke-Ernzerhof (PBE) functional within the generalized gradient approximation (GGA) was employed to describe the exchange-correlation interaction [54]. The DFT+U approach was used to correct for on-site Coulomb interactions of localized 3d electrons, with U_{eff} = 3.1 eV for Mn and 6.2 eV for Ni [55].

Structural optimizations were performed for each structure using computational parameters consistent with Materials Project Settings as implemented in Pymatgen, followed by a static energy calculation [56]. The final static runs used a 520 eV cutoff and a reciprocal density of approximately 64 k-points $Å^{-3}$. Electronic convergence was set to 10^{-6} eV. These static-run energies were used to calculate the site energies for the Na vacancies.

Molecular dynamics (MD) simulations were performed using the LAMMPS package with the TensorNet-MatPES-PBE-v2025.1-PES foundation potential to investigate Na-ion diffusion [57–59] All simulations were carried out in the NPT ensemble using a

Nosé-Hoover thermostat to maintain the target temperature [60, 61] The time step was set to 1 fs, and each trajectory was equilibrated for 500 ps followed by a 1 ns production run for diffusion analysis.

A 600-atom supercell was used in each case for the diffusion analysis, with Na-ion diffusivities computed from MD trajectories between 1200 and 1500 K using the Nernst-Einstein equation based on mean-squared displacements. The temperature-dependent diffusion coefficients were fitted to an Arrhenius plot, and the extrapolated 300 K ionic diffusivity was obtained to evaluate room-temperature transport behavior.

Acknowledgements

The authors acknowledge the use of the following facilities at the University of Chicago: The X-ray Research Facilities in the Department of Chemistry, and the Materials Research Science and Engineering Center (MRSEC). The TEM was performed on Thermo Fisher Scientific Spectra Ultra X lliad which was developed and supported as part of a CRADA #01300710 and CRADA #A24560 among Argonne National Laboratory, University of Chicago and Thermo Fisher Scientific.For synchrotron XRD measurements, this research was performed on APS beam time (17 BM) from the Advanced Photon Source, a U.S. Department of Energy (DOE) Office of Science user facility operated for the DOE Office of Science by Argonne National Laboratory under Contract No. DE-AC02-06CH11357. For hard XAS measurements, this research used resources (7-BM-B) of the National Synchrotron Light Source II, a U.S. Department of Energy (DOE) Office of Science User Facility operated for the DOE Office of Science by Brookhaven National Laboratory under Contract No. DE-SC0012704. For soft XAS and RIXS measurements, the research used resources of the Advanced Light Source (beamline 8.0.1.1), a U.S. DOE Office of Science User Facility under contract no. DE-AC02-05CH11231. A R. Mishra and S. P. Ong acknowledge funding from the Shell Global Solutions Inc. (contract no. CW649697) for the computational studies. This work used Expanse at San Diego Supercomputer Center through allocation DMR150014 from the Advanced Cyberinfrastructure Coordination Ecosystem: Services & Support (ACCESS) program, which is supported by U.S. National Science Foundation grants #2138259, #2138286, #2138307, #2137603, and #2138296.This work was funded by TCG Centers for Research and Education in Science and Technology (FRA001320). Y.S. Meng acknowledges partial support from the Energy Technologies initiative at the University of Chicago's Institute for Climate and Sustainable Growth.

Funding

This work was supported by TCG Centers for Research and Education in Science and Technology. Y.S. Meng acknowledges partial support from the Energy Technologies initiative at the University of Chicago's Institute for Climate and Sustainable Growth.

Conflicts of Interest

The authors declare no conflicts of interest.

Data Availability Statement

The data that support the findings of this study are available in the supplementary material of this article.

References

1. P. Zhai, M. Xia, Y. Wu, et al., "Engineering Single-atomic Ruthenium Catalytic Sites on Defective Nickel-iron Layered Double Hydroxide for Overall Water Splitting," *Nature Communications* 12 (2021): 4587.

2. X. Fu, D. N. Beatty, G. G. Gaustad, et al., "Perspectives on Cobalt Supply through 2030 in the Face of Changing Demand," *Environmental Science & Technology* 54 (2020): 2985–2993.

3. B. Ravi, K. Bhuwalka, E. A. Moore, et al., "Clean Energy Demand Must Secure Sustainable Nickel Supply," *Joule* 8, no. 11 (2024): 2960–2973, https://doi.org/10.1016/j.joule.2024.10.008.

4. P. K. Nayak, L. Yang, W. Brehm, and P. Adelhelm, "From Lithium-Ion to Sodium-Ion Batteries: Advantages, Challenges, and Surprises," *Angewandte Chemie International Edition* 57 (2018): 102–120.

5. J. M. Tarascon, "Na-ion versus Li-Ion Batteries: Complementarity Rather than Competitiveness," *Joule* 4 (2020): 1616, https://doi.org/10.1016/j.joule.2020.06.003.

6. H. S. Hirsh, Y. Li, D. H. S. Tan, et al., "Sodium-Ion Batteries Paving the Way for Grid Energy Storage," *Advanced Energy Materials* 10 (2020): 2001274.

7. A. Rudola, R. Sayers, C. J. Wright, and J. Barker, "Opportunities for Moderate-range Electric Vehicles Using Sustainable Sodium-Ion Batteries," *Nature Energy* 8 (2023): 215–218.

8. J. Liu, J. Xiao, J. Yang, et al., "The TWh Challenge: Next Generation Batteries for Energy Storage and Electric Vehicles," *Next Energy* 1 (2023): 100015.

9. B. Sayahpour, H. Hirsh, S. Parab, L. H. B. Nguyen, M. Zhang, and Y. S. Meng, "Perspective: Design of Cathode Materials for Sustainable Sodium-Ion Batteries," *MRS Energy & Sustainability* 9 (2022): 183–197.

10. S. Mariyappan, Q. Wang, and J. M. Tarascon, "Will Sodium Layered Oxides Ever Be Competitive for Sodium Ion Battery Applications?," *Journal of The Electrochemical Society* 165 (2018): A3714–A3722.

11. W. Zuo, A. Innocenti, M. Zarrabeitia, D. Bresser, Y. Yang, and S. Passerini, "Layered Oxide Cathodes for Sodium-Ion Batteries: Storage Mechanism, Electrochemistry, and Techno-economics," *Accounts of Chemical Research* 56 (2023): 284–296.

12. C. Delmas, C. Fouassier, and P. Hagenmuller, "Structural Classification and Properties of the Layered Oxides," *Physica B+C* 99 (1980): 81–85.

13. N. A. Katcho, J. Carrasco, D. Saurel, et al., "Origins of Bistability and Na Ion Mobility Difference in P2- and O3-Na 2/3 Fe 2/3 Mn 1/3 O 2 Cathode Polymorphs," *Advanced Energy Materials* 7 (2017): 1601477.

14. C. Zhao, Q. Wang, Z. Yao, et al., "Rational Design of Layered Oxide Materials for Sodium-Ion Batteries," *Science* 370 (2020): 708–711.

15. R. J. Clément, P. G. Bruce, and C. P. Grey, "Review—Manganese-Based P2-Type Transition Metal Oxides as Sodium-Ion Battery Cathode Materials," *Journal of the Electrochemical Society* 162 (2015): A2589, https://doi.org/10.1149/2.0201514jes.

16. Y. Shi, P. Jiang, S. Wang, et al., "Slight Compositional Variation-Induced Structural Disorder-to-Order Transition Enables Fast Na+ Storage in Layered Transition Metal Oxides," *Nature Communications* 13 (2022): 7888, https://doi.org/10.1038/s41467-022-35597-4.

17. C. Zhao, Z. Yao, Q. Wang, et al., "Revealing High Na-Content P2-Type Layered Oxides as Advanced Sodium-Ion Cathodes," *Journal of the American Chemical Society* 142 (2020): 5742–5750.

18. P. F. Wang, H. R. Yao, X. Y. Liu, et al., "Na+/Vacancy Disordering Promises High-Rate Na-Ion Batteries," *Science Advances* 4 (2018): aar6018, https://doi.org/10.1126/sciadv.aar6018.

19. M. M. Rahman, S. McGuigan, S. Li, et al., "Chemical Modulation of Local Transition Metal Environment Enables Reversible Oxygen Redox in Mn-Based Layered Cathodes," *ACS Energy Letters* 6 (2021): 2882–2890.

20. L. Yang, S. H. Luo, Y. Wang, et al., "Cu-Doped Layered P2-type Na0.67Ni0.33-xCuxMn0.67O2 Cathode Electrode Material with Enhanced Electrochemical Performance for Sodium-Ion Batteries," *Chemical Engineering Journal* 404 (2021): 126578.

21. J. Xu, D. H. Lee, R. J. Clément, et al., "Identifying the Critical Role of Li Substitution in P2–Na X [Li y Ni z Mn 1– y—z]O 2 (0 < x , y , z

< 1) Intercalation Cathode Materials for High-Energy Na-Ion Batteries," *Chemistry of Materials* 26 (2014): 1260–1269.

22. L. Zheng, J. Li, and M. N. Obrovac, "Crystal Structures and Electrochemical Performance of Air-Stable Na 2/3 Ni 1/3– x Cu X Mn 2/3 O 2 in Sodium Cells," *Chemistry of Materials* 29 (2017): 1623–1631.

23. Y. Li, Z. Yang, S. Xu, et al., "Air-Stable Copper-Based P2-Na7/9Cu2/9Fe1/9Mn2/3O2 as a New Positive Electrode Material for Sodium-Ion Batteries," *Advanced Science* 2 (2015): 1500031, https://doi.org/10.1002/advs.201500031.

24. B. Xiao, X. Liu, X. Chen, et al., "Uncommon Behavior of Li Doping Suppresses Oxygen Redox in P2-Type Manganese-Rich Sodium Cathodes," *Advanced Materials* 33 (2021): 2107141.

25. E. Grépin, Y. Zhou, B. Li, G. Rousse, J. M. Tarascon, and S. Mariyappan, "Optimal Ti-Substitution in Layered Oxide Cathodes for Na-Ion Batteries," *Chemistry of Materials* 36, no. 21 (2024): 10804–10812, https://doi.org/10.1021/acs.chemmater.4c02501.

26. M. J. W. Ogley, A. S. Menon, G. C. Pandey, et al., "Metal-ligand Redox in Layered Oxide Cathodes for Li-Ion Batteries," *Joule* 9 (2025): 101775.

27. R. A. House, U. Maitra, M. A. Pérez-Osorio, et al., "Superstructure Control of First-Cycle Voltage Hysteresis in Oxygen-Redox Cathodes," *Nature* 577 (2020): 502–508.

28. C. Ma, J. Alvarado, J. Xu, et al., "Exploring Oxygen Activity in the High Energy P2-Type Na 0.78 Ni 0.23 Mn 0.69 O 2 Cathode Material for Na-Ion Batteries," *Journal of the American Chemical Society* 139 (2017): 4835–4845.

29. B. Mortemard De Boisse, G. Liu, J. Ma, et al., "Intermediate Honeycomb Ordering to Trigger Oxygen Redox Chemistry in Layered Battery Electrode," *Nature Communications* 7 (2016): 11397.

30. C. Cheng, M. Ding, T. Yan, et al., "Anionic Redox Activities Boosted by Aluminum Doping in Layered Sodium-Ion Battery Electrode," *Small Methods* 6 (2022): 2101524.

31. H. Zhu, Z. Yao, H. Zhu, et al., "Unblocking Oxygen Charge Compensation for Stabilized High-Voltage Structure in P2-Type Sodium-Ion Cathode," *Advanced Science* 9 (2022): 2200498.

32. J. Xu, M. Sun, R. Qiao, et al., "Elucidating Anionic Oxygen Activity in Lithium-Rich Layered Oxides," *Nature Communications* 9, no. 1 (2018): 947, https://doi.org/10.1038/s41467-018-03403-9.

33. Y. Tang, Q. Zhang, W. Zuo, et al., "Sustainable Layered Cathode with Suppressed Phase Transition for Long-Life Sodium-Ion Batteries," *Nature Sustainability* 7 (2024): 348–359.

34. S. Jia, M. Abdolhosseini, Y. Li, et al., "Promoting Reversible Anionic Redox in Sodium-Ion Cathodes by Doping and Phase Control," *ACS Materials Letters* 7 (2025): 1370–1377.

35. J. Wandt, A. T. S. Freiberg, A. Ogrodnik, and H. A. Gasteiger, "Singlet Oxygen Evolution from Layered Transition Metal Oxide Cathode Materials and Its Implications for Lithium-ion Batteries," *Materials Today* 21 (2018): 825–833.

36. M. Luo, S. Zheng, J. Wu, et al., "Identifying the Anionic Redox Activity in Cation-Disordered Li 1.25 Nb 0.25 Fe 0.50 O_2 /C Oxide Cathodes for Li-Ion Batteries," *Journal of Materials Chemistry A* 8 (2020): 5115–5127.

37. H. Zheng, M. Fan, C. Zhang, W. He, G. Gao, Y. Liu, L. Wang, Q. Xie, D. L. Peng, and J. Lu, *Advanced Materials* 37 (2025): 2414443.

38. S. Li, Z. Liu, L. Yang, et al., "Anionic Redox Reaction and Structural Evolution of Ni-Rich Layered Oxide Cathode Material," *Nano Energy* 98 (2022): 107335.

39. R. Jung, M. Metzger, F. Maglia, C. Stinner, and H. A. Gasteiger, "Oxygen Release and Its Effect on the Cycling Stability of LiNi X Mn y Co Z O 2 (NMC) Cathode Materials for Li-Ion Batteries," *Journal of The Electrochemical Society* 164 (2017): A1361–A1377.

40. S. Thekkekara, P. Tripathi, J. M. Sudharma, et al., "Boosting the Structural Stability of High-Voltage Sodium Layered Cathodes via Site-Selective La/Ti Co-Doping," *Small* 21 (2025): 2502341.

41. D. H. Seo, J. Lee, A. Urban, R. Malik, S. Kang, and G. Ceder, "The Structural and Chemical Origin of the Oxygen Redox Activity in Layered and Cation-disordered Li-Excess Cathode Materials," *Nature Chemistry* 8 (2016): 692–697.

42. G. Assat, A. Iadecola, D. Foix, R. Dedryvere, and J. M. Tarascon, "Direct Quantification of Anionic Redox over Long Cycling of Li-Rich NMC via Hard X-ray Photoemission Spectroscopy," *ACS Energy Letters* 3 (2018): 2721–2728.

43. K. Luo, M. R. Roberts, R. Hao, et al., "Charge-Compensation in 3d-Transition-Metal-Oxide Intercalation Cathodes through the Generation of Localized Electron Holes on Oxygen," *Nature Chemistry* 8 (2016): 684–691.

44. Z. Li, W. Kong, Y. Yu, et al., "Tuning Bulk O 2 and Nonbonding Oxygen State for Reversible Anionic Redox Chemistry in P2-Layered Cathodes," *Angewandte Chemie International Edition* 61 (2022): 202115552.

45. H. Van Nguyen, H. T. N. Nguyen, N. L. T. Huynh, A. L. B. Phan, M. Van Tran, and P. M. L. Le, "A Study of the Electrochemical Kinetics of Sodium Intercalation in P2/O1/O3-NaNi1/3Mn1/3Co1/3O2," *Journal of Solid State Electrochemistry* 24 (2019): 57–67.

46. Z. Cheng, B. Zhao, Y. J. Guo, et al., "Mitigating the Large-Volume Phase Transition of P2-Type Cathodes by Synergetic Effect of Multiple Ions for Improved Sodium-Ion Batteries," *Advanced Energy Materials* 12 (2022): 2103461.

47. L. Zou, J. Zhong, Q. Wei, et al., "Enabling Rapid and Stable Sodium Storage via a P2-Type Layered Cathode with High-Voltage Zero-Phase Transition Behavior," *Small* 20 (2024): 2400315.

48. J. W. Somerville, A. Sobkowiak, N. Tapia-Ruiz, et al., "Nature of the "Z"-Phase in Layered Na-Ion Battery Cathodes," *Energy & Environmental Science* 12 (2019): 2223–2232.

49. R. J. Clément, J. Billaud, A. Robert Armstrong, et al., "Structurally Stable Mg-doped P2-Na 2/3 Mn 1– y Mg y O 2 Sodium-ion Battery Cathodes with High Rate Performance: Insights from Electrochemical, NMR and Diffraction Studies," *Energy & Environmental Science* 9, no. 10 (2016): 3240–3251, https://doi.org/10.1039/C6EE01750A.

50. L. Liu, X. Li, S. H. Bo, et al., "High-Performance P2-Type Na 2/3 (Mn 1/2 Fe 1/4 Co 1/4)O 2 Cathode Material with Superior Rate Capability for Na-Ion Batteries," *Advanced Energy Materials* 5 (2015): 1500944.

51. J. Kim, S. Park, S. Hwang, and W. S. Yoon, "Principles and Applications of Galvanostatic Intermittent Titration Technique for Lithium-Ion Batteries," *Journal of Electrochemical Science and Technology* 13 (2021): 19–31.

52. G. Kresse and J. Furthmüller, "Efficient Iterative Schemes for Ab Initio Total-Energy Calculations Using a Plane-wave Basis Set," *Physical Review B* 54 (1996): 11169–11186.

53. P. E. Blöchl, "Projector Augmented-Wave Method," *Physical Review B* 50 (1994): 17953, https://doi.org/10.1103/PhysRevB.50.17953.

54. J. P. Perdew, K. Burke, and M. Ernzerhof, "Generalized Gradient Approximation Made Simple," *Physical Review Letters* 77 (1996): 3865–3868.

55. S. L. Dudarev, G. A. Botton, S. Y. Savrasov, C. J. Humphreys, and A. P. Sutton, "Electron-Energy-Loss Spectra and the Structural Stability of Nickel Oxide: an LSDA+U Study," *Physical Review B* 57 (1998): 1505–1509.

56. S. P. Ong, W. D. Richards, A. Jain, et al., "Python Materials Genomics (pymatgen): A Robust, Open-source Python Library for Materials Analysis," *Computational Materials Science* 68 (2013): 314–319.

57. S. Plimpton, "Fast Parallel Algorithms for Short-Range Molecular Dynamics," *Journal of Computational Physics* 117 (1995): 1–19.

58. A. D. Kaplan, R. Liu, J. Qi, et al., "A Foundational Potential Energy Surface Dataset for Materials," *arXiv* (2025), https://arxiv.org/abs/2503.04070.

59. T. W. Ko, B. Deng, M. Nassar, et al., "Materials Graph Library (MatGL), an Open-source Graph Deep Learning Library for Materials Science and Chemistry," *Npj Computational Materials* 11 (2025): 253.

60. S. Nosé and S. Nosi, "A Molecular Dynamics Method for Simulations in the Canonical Ensemble," *Molecular Physics* 52 (1984): 255, https://doi.org/10.1080/00268970110089108.

61. W. G. Hoover, "Canonical Dynamics: Equilibrium Phase-space Distributions," *Physical Review A* 31 (1985): 1695–1697.

Supporting Information

Additional supporting information can be found online in the Supporting Information section.

Supporting File: aenm70720-sup-0001-SuppMat.docx.